

35870  
1.315.07

# ATTITUDE DETERMINATION IMPROVEMENTS FOR GOES

John L. Crassidis  
Catholic University of America  
Dept. of Mech. Eng.  
Washington, D.C. 20064

F. Landis Markley, Arthur M. Kyle  
Goddard Space Flight Center  
Guidance and Control Branch, Code 712  
Greenbelt, MD 20771

Kathie Kull  
Orbital Sciences Corporation  
Greenbelt, MD 20770

## Abstract

In this paper, a summary of the basic simulation parameters and results of a new study for the Geostationary Operational Environmental Satellite (GOES) is shown. The study for GOES involves the simulation of minor modifications to the current spacecraft, so that the relative performance of these modifications can be analyzed. The first modification studied requires the placement of a baseline inertial reference unit, such as the Dry Rotor Inertia Reference Unit (DRIRU-II) or the Hemispherical Resonator Gyro (HRG), onto the spacecraft. The imager/sounder assembly is currently used to obtain landmark and/or star observations in order to compensate for spacecraft motions and external disturbances through ground processing. The study utilizes the imager/sounder assembly as another attitude sensor for on-board attitude determination. Also, the addition of star trackers is used to provide precise attitude knowledge.

## Introduction

The current (GOES I-M) spacecraft specification for the knowledge requirement is  $112 \mu\text{rad}$ . This requirement is met through ground processing 99% of the time in the east/west direction and 95% of the time in the north/south direction. The spacecraft specification for the within-frame registration is  $42 \mu\text{rad}$ . The current spacecraft uses an Earth Sensor Assembly (ESA) to provide roll and pitch information. Yaw knowledge is not sensed. However, yaw control is achieved through roll/yaw coupling. A set of gyros based on the Digital Integration Rate Assembly (DIRA) also is on the current spacecraft. However, the DIRA has an operational lifetime of 2000 hours. Therefore, the on-board gyros are not used for mission mode attitude determination and control.

An outline of the remainder of this paper proceeds as follows. First, the simulation model for the gyro, the ESA, and the imager/sounder assembly are shown. This includes the simulation parameters used for Earth clouds and Earth radiance/gradients effects in the ESA, and non-repeatable errors in the imager/sounder assembly. Then, the simulated attitude sensor and gyro measurements are used in a Kalman filter for attitude determination. Results are presented for two

cases: 1) using the ESA, and 2) using both the ESA and imager/sounder assembly. Next, results using a star tracker are shown. This includes simulation results with and without the addition of gyros. Finally, conclusions are stated based on the simulation results.

## Earth Sensor, Imager/Sounder

In this section, a brief overview of the simulation parameters for the gyro model, the ESA model, and the imager/sounder model is shown. The true angular velocity is assumed to be modeled by [1]

$$\underline{\omega} = \underline{\tilde{\omega}}_g - \underline{b} - \underline{\eta}_1 \quad (1)$$

where  $\underline{\omega}$  is the true angular velocity,  $\underline{\tilde{\omega}}_g$  is the gyro-determined angular velocity, and  $\underline{b}$  is the gyro drift vector,

$$\underline{\dot{b}} = \underline{\eta}_2 \quad (2)$$

The  $3 \times 1$  vectors,  $\underline{\eta}_1$  and  $\underline{\eta}_2$ , are assumed to be modeled by a Gaussian white-noise process with

$$E\{\underline{\eta}_i(t)\} = \underline{0} \quad i = 1, 2 \quad (3)$$

$$E\{\underline{\eta}_i(t)\underline{\eta}_j^T(t')\} = Q_i \delta_{ij} \delta(t-t') \quad i, j = 1, 2 \quad (4)$$

where

$$Q = \begin{bmatrix} \sigma_v^2 I_{3 \times 3} & 0_{3 \times 3} \\ 0_{3 \times 3} & \sigma_u^2 I_{3 \times 3} \end{bmatrix} \quad (5)$$

The DRIRU-II drift-rate noise and measurement noise characteristics are given by  $\sigma_u = 2.15 \times 10^{-4} \mu\text{rad}/\text{sec}^{3/2}$  and  $\sigma_v = 0.206 \mu\text{rad}/\text{sec}^{1/2}$ . The nominal motion of the spacecraft involves a rotation once per orbit about the spacecraft's y-axis. Therefore, the nominal angular velocity is given by

$$\underline{\omega} = \begin{bmatrix} 0 \\ \omega_n \\ 0 \end{bmatrix} \quad (6)$$

where  $\omega_n$  is the orbit rotation ( $7.27 \times 10^{-5}$  rad / sec).

The ESA measures the spacecraft's roll and pitch angles. These angles are measured with respect to a moving Earth frame. The gyros provide attitudes with respect to an inertially fixed frame (e.g., GCI). Since the body rotation axis is about the spacecraft's y-axis, the body measurement vector is given by [2]

$$\underline{B}_e = \begin{bmatrix} -\sin(p)\cos(r) \\ \sin(r) \\ \cos(p)\cos(r) \end{bmatrix} \quad (7)$$

where  $r$  and  $p$  are the scanner roll and pitch angles, respectively. The inertial reference vector is given by

$$\underline{I}_e = A^T(q)\underline{B}_e \quad (8)$$

where  $q$  is the true quaternion (obtained by kinematic propagation using the true angular velocity). The ESA "measurements" are obtained by using the following model

$$\tilde{p} = p + v_p + w_p \quad (9)$$

where  $v_p$  is a zero-mean Gaussian process with a  $3\sigma$  value of 0.02 degrees, and  $w_p$  represents the non-repeatable errors due to Earth cloud and Earth radiance/gradients effects. The non-repeatable error is assumed to be modeled by the following discrete process

$$w_p(i+1) = A w_p(i) + L(1 - A^2)^{1/2} g(i) \quad (10a)$$

$$A = \exp(-4 \Delta t B) \quad (10b)$$

where  $\Delta t$  is the sampling interval (0.25 seconds for the ESA),  $B$  is the bandwidth (for weather purposes, this set to about 1/6 days),  $L$  is the  $1\sigma$  amplitude (experience has shown that this is about 200  $\mu$ rad), and  $g$  is a zero-mean normal Gaussian process. This same error model is applied to the Earth roll "measurement." Since the roll and pitch measurements from the Earth sensor are small, the body measurements can be approximated by

$$\underline{\tilde{B}}_B^e = \begin{bmatrix} -\tilde{p} \\ \tilde{r} \\ 1 \end{bmatrix} \quad (11)$$

The imager/sounder assembly can measure stars in a  $23^\circ$  E/W  $\times$   $21^\circ$  N/S field of view, outside of the Earth limb. The orbit-attitude tracking system contains a catalog of bright stars visible by the imager/sounder which can sense three stars at 45 second intervals. For simulation purposes these stars are assumed to be found in different quadrants in the field of view. The imager/sounder star windows are staggered so that the data is acquired every 15 minutes. The imager/sounder measures the tangent of two angles,  $\beta_1$  and  $\beta_2$ , resulting in a body vector given by [2]

$$\underline{B}_{i/s} = \frac{1}{\sqrt{1 + \tan^2 \beta_1 + \tan^2 \beta_2}} \begin{bmatrix} \tan \beta_1 \\ \tan \beta_2 \\ 1 \end{bmatrix} \quad (12)$$

The imager/sounder "measurements" are obtained by using the following model

$$\tan \tilde{\beta}_i = \tan \beta_i + v_{b_i} + w_{b_i}, \quad i = 1, 2 \quad (13)$$

where  $v_b$  is a zero-mean Gaussian process with a  $3\sigma$  value of 28  $\mu$ rad. The non-repeatable error in the imager/sounder is assumed to be modeled by the following process

$$\dot{\underline{x}} = \begin{bmatrix} 0 & 1 \\ -\omega_n^2 & 0 \end{bmatrix} \underline{x} + \begin{bmatrix} 0 \\ 1 \end{bmatrix} \eta \quad (14a)$$

$$w_b = [1 \ 0] \underline{x} \quad (14b)$$

where  $\eta$  is a zero-mean Gaussian process. The standard deviation of  $\eta$  is selected such that the output of  $w_b$  has a  $3\sigma$  value of about 200  $\mu$ rad.

## Simulation Results

For this part of the study, an investigation of the relative performance between using on-board gyros and without the use of gyros was examined. For the on-board gyro case, a standard Kalman filter with a gyro propagated model was used for attitude determination. The simulations were run for six cases, which include: 1) ESA only with no non-repeatable (NR) errors, 2) ESA only with NR errors, 3) ESA and imager/sounder (I/S) with no NR ESA errors and no NR I/S errors, 4) ESA and I/S with no NR ESA errors and with NR I/S errors, 5) ESA and I/S with NR ESA errors and no NR I/S errors, and 6) ESA and I/S with both NR ESA errors and NR I/S errors.

The first two cases involve using the ESA only. A plot of a typical non-repeatable (radiance/gradients) error effect is shown in Figure 1. From this plot, the magnitude of the error is seen to be about 200  $\mu$ rad. A Monte Carlo type analysis shows that 200-250  $\mu$ rad is about the  $3\sigma$  range for this error. Error angle plots for the first two cases are shown in Figures

2 and 3. With no NR errors in the ESA, the attitude accuracy is within 60  $\mu\text{rad}$ . With the NR errors in the ESA, this accuracy is degraded to about 200  $\mu\text{rad}$ . The large errors in the yaw angle estimates are due to filter un-observability. The observability of using an ESA combined with gyro measurements in a Kalman filter can be shown by using the simplifying assumption of a constant coefficient system. The state vector in the Kalman filter is given by [1]

$$\Delta \underline{x} = \begin{bmatrix} \Delta \underline{\alpha} \\ \Delta \underline{b} \end{bmatrix} \quad (15)$$

where  $\Delta \underline{\alpha}$  is a  $3 \times 1$  angle error vector (roll, pitch, yaw), and  $\Delta \underline{b}$  is a  $3 \times 1$  gyro-bias error vector. The system error equations, state matrix and sensitivity matrix are given by

$$\begin{aligned} \Delta \dot{\underline{x}} &= F \Delta \underline{x} + G \Delta \eta \\ \Delta \underline{z} &= H \Delta \underline{x} + \Delta \nu \end{aligned} \quad (16a)$$

$$F = \begin{bmatrix} -[\underline{\omega} \times] & -I_{3 \times 3} \\ 0_{3 \times 3} & 0_{3 \times 3} \end{bmatrix} \quad (16b)$$

$$H = \left[ \left[ A(\underline{q}) \underline{B}_I^e \times \right] \ ; \ 0_{3 \times 3} \right] \quad (16c)$$

where the angular velocity vector ( $\underline{\omega}$ ) is given by Equation (6), and  $[\underline{\omega} \times]$  is the cross product matrix. Therefore, the state error angle equations are given by

$$\Delta \dot{\alpha}_1 = -\omega_n \Delta \alpha_3 - \Delta b_1 \quad (17a)$$

$$\Delta \dot{\alpha}_2 = -\Delta b_2 \quad (17b)$$

$$\Delta \dot{\alpha}_3 = \omega_n \Delta \alpha_1 - \Delta b_3 \quad (17c)$$

The first and third equations show the coupling effects between roll and yaw. The nominal body measurements for the ESA are given by

$$V = \begin{bmatrix} 0 & -1 & -2.64 \times 10^{-5} & 0 & 0 & 0 \\ 0 & -2.64 \times 10^{-5} & 1 & 0 & 0 & 0 \\ 7.27 \times 10^{-5} & 0 & 0 & 0 & 0 & 1 \\ 1 & 0 & 0 & 0 & 0 & -7.27 \times 10^{-5} \\ 0 & 0 & 0 & 1 & 0 & 0 \\ 0 & 0 & 0 & 0 & -1 & 0 \end{bmatrix} \quad (22)$$

$$\underline{B}_B^e = A(\underline{q}) \underline{B}_I^e = \begin{bmatrix} 0 \\ 0 \\ 1 \end{bmatrix} \quad (18)$$

which reflects the fact that the spacecraft is Earth-pointing. From Equations (16)-(18), the state matrix ( $F$ ) and sensitivity matrix ( $H$ ) are now constant.

The observability matrix is given by

$$O = \begin{bmatrix} H \\ HF \\ HF^2 \\ \vdots \\ HF^5 \end{bmatrix} \quad (19)$$

which is an  $18 \times 6$  dimensional matrix. This matrix must be rank 6 for the system to be fully observable. However, using the system matrices in Equation (16) yields a rank 5 observability matrix. A singular value decomposition (SVD) of the observability matrix can provide an insight to which states are observable, as well as the degree of observability. The SVD of Equation (19) is given by

$$U S V^T = O \quad (20)$$

where  $S$  is an  $18 \times 6$  diagonal matrix, and  $U$  and  $V$  are unitary matrices with dimensions  $18 \times 18$  and  $6 \times 6$ , respectively. The diagonal elements of the first 6 rows of  $S$  yield the singular values of the system. These singular values yield the degree of observability, which is determined to be

$$S = \begin{bmatrix} 1 \\ 1 \\ 1 \\ 1 \\ 7.27 \times 10^{-5} \\ 0 \end{bmatrix} \quad (21)$$

The columns of  $V$  shows which states are observable, and also show the degree of cross correlated observability in the states. This matrix is determined to be

The first four columns of  $V$  correspond to completely observable states. The second and third columns of  $V$  indicate that the roll and pitch angle states are completely observable. Also, there is some correlation between these states, shown by the  $-2.64 \times 10^{-5}$  term. The sixth column of  $V$  is associated with a singular value of zero. This shows that the yaw angle state is not observable. This reflects a higher covariance in the yaw angle estimate, as compared to the roll and pitch angle covariances (see Figure 4). The fourth column of  $V$  corresponds to the pitch drift-rate state, which is completely observable, since its associated singular value is one. The fifth column of  $V$  corresponds to the yaw drift-rate state, which is weakly observable, since its associated singular value is small (i.e.,  $7.27 \times 10^{-5}$ ). However, this state is completely decoupled from any other

state. The first column of  $V$ , as well as the sixth column, shows the coupling between the yaw angle state and the roll drift-rate state (due to quarter-orbit coupling). This indicates that the error in this state is attributed to both actual roll rate errors and yaw angle errors. Since the yaw angle state is not observable, the roll drift-rate errors and yaw angle errors cannot be separated. A plot of the gyro drift-rate covariances is shown in Figure 5. The error covariance of the roll drift-rate state is larger than the yaw drift-rate error covariance. This is most likely due to the fact the yaw angle errors cannot be separated from the roll drift-rate error.

Plots of the four remaining cases, which include the imager/sounder as an attitude sensor, are shown in Figure 6-9. A summary of the results for all cases is shown in Table 1.

Table 1 Attitude Errors for Various Sensor Configurations and Error Sources

Case	Error Sources	Roll Errors	Pitch Errors	Yaw Errors
1	no NR ESA	60 $\mu$ rad	60 $\mu$ rad	$1 \times 10^5$ $\mu$ rad
2	NR ESA	200 $\mu$ rad	200 $\mu$ rad	$1 \times 10^5$ $\mu$ rad
3	no NR ESA, no NR I/S	60 $\mu$ rad	60 $\mu$ rad	200 $\mu$ rad
4	no NR ESA, NR I/S	100 $\mu$ rad	100 $\mu$ rad	200 $\mu$ rad
5	NR ESA, no NR I/S	100 $\mu$ rad	100 $\mu$ rad	200 $\mu$ rad
6	NR ESA, NR I/S	200 $\mu$ rad	200 $\mu$ rad	300 $\mu$ rad

Since the imager/sounder can measure stars which are off nadir, yaw angle information is possible. From Table 1, using the imager/sounder as another sensor significantly improves the yaw angle estimate. Also, since the magnitude of the non-repeatable errors is assumed to be approximately the same in the ESA and in the imager/sounder assembly, the attitude errors are also approximately equal when adding these errors to each sensor individually (i.e., case four and five). The sixth case involves using both the ESA and imager/sounder assembly with non-repeatable errors added to each sensor. A purely deterministically found attitude using the QUEST method yields errors which are approximately the same magnitude as case six (see Figure 10). Therefore, the addition of gyros does not seem to significantly improve the attitude accuracy.

In order to possibly estimate the non-repeatable effects in the imager/sounder, a colored noise Kalman filter was developed. An analysis can be performed by expanding upon Farrenkopf's model. The assumed model for the colored-noise Farrenkopf analysis is given by [3]

$$\dot{\theta} = \bar{\omega}_g - \eta_v - b \quad (23a)$$

$$\dot{b} = \eta_u \quad (23b)$$

$$\dot{\underline{l}} = A_l \underline{l} + B_l \eta_l \quad (23c)$$

where  $\theta$  is the scalar (single-axis) attitude angle,  $\bar{\omega}_g$  is the gyro output,  $b$  is the gyro-drift rate,  $\underline{l}$  is the colored-noise output,  $\eta_v$ ,  $\eta_u$ , and  $\eta_l$  are zero-mean Gaussian processes with standard deviations of  $\sigma_v$ ,  $\sigma_u$ , and  $\sigma_l$ , respectively, and  $A_l$  and  $B_l$  are the colored-noise system matrices, given by

$$A_l = \begin{bmatrix} 0 & 1 \\ -\omega_n^2 & 0 \end{bmatrix} \quad (24a)$$

$$B_l = \begin{bmatrix} 0 \\ 1 \end{bmatrix} \quad (24b)$$

where  $\omega_n$  is set to orbit rate. Therefore, the full continuous system matrix from Equations (23) and (24) is given by

$$F = \begin{bmatrix} 0 & -1 & 0 & 0 \\ 0 & 0 & 0 & 0 \\ 0 & 0 & 0 & 1 \\ 0 & 0 & -\omega_n^2 & 0 \end{bmatrix} \quad (25)$$

with the state-transition matrix of  $F$  denoted by  $\Phi$ . The measurement model is given by

$$\tilde{y} = H \begin{bmatrix} \theta \\ b \\ l \end{bmatrix} + v \quad (26)$$

where  $v$  is a zero-mean Gaussian process with covariance  $r$ , and  $H$  is given by

$$H = [1 \ 0 \ 1 \ 0] \quad (27)$$

Equations (26) and (27) show that the colored-noise is added to the measurement. The state-noise covariance matrix can be computed as

$$Q = \begin{bmatrix} \sigma_v^2 \Delta t + 1/3 \sigma_u^2 \Delta t^3 & -1/2 \sigma_u^2 \Delta t^2 & 0 & 0 \\ -1/2 \sigma_u^2 \Delta t^2 & \sigma_u^2 \Delta t & 0 & 0 \\ 0 & 0 & 0 & 0 \\ 0 & 0 & 0 & \sigma_l^2 \Delta t \end{bmatrix} \quad (28)$$

where  $\Delta t$  is the sampling interval. The steady-state error covariance just subsequent to an update is given by

$$P = \Phi P \Phi^T - P H^T [H P H^T + r]^{-1} H P + Q \quad (29)$$

which can be solved using an eigenvector decomposition of the Hamiltonian matrix, where  $\Phi$  is the state transition matrix of Equation (25).

The standard deviation of the colored-noise input varies from  $\sigma_l = 1 \times 10^{-7} \mu\text{rad}$  to  $\sigma_l = 1 \times 10^{-5} \mu\text{rad}$ , which corresponds to a colored-noise magnitude ranging from  $15 \mu\text{rad}$  to  $1800 \mu\text{rad}$  (these are  $3\sigma$  values). This colored-noise output simulates the non-repeatable effect in the imager/sounder assembly. A plot of the steady-state colored-noise attitude accuracy is shown in Figure 11. Note that the standard Farrenkopf analysis with no colored-noise gives an attitude accuracy of  $56 \mu\text{rad}$  ( $3\sigma$  value), which is similar to the results shown in Figure 6. This colored-noise analysis shows that using an *accurate* model for the non-repeatable errors can reduce the attitude errors when using a Kalman

filter. However, an analysis using actual data should be performed to investigate the validity of this approach.

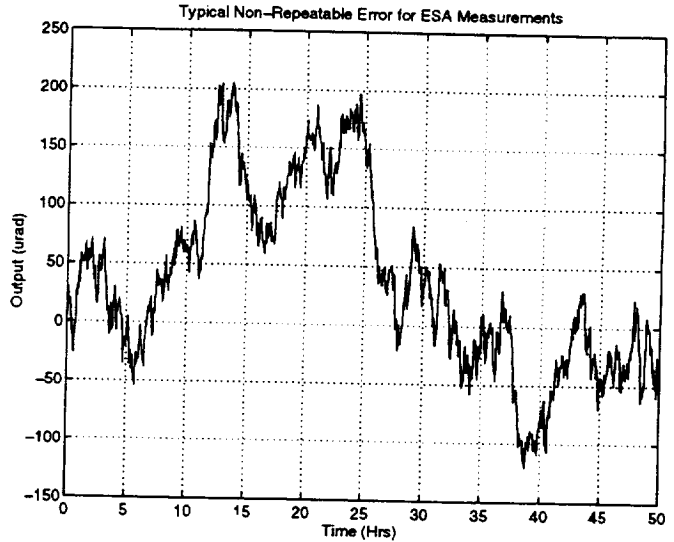


**Figure 1 Non-Repeatable Errors for the ESA in Both Roll and Pitch**

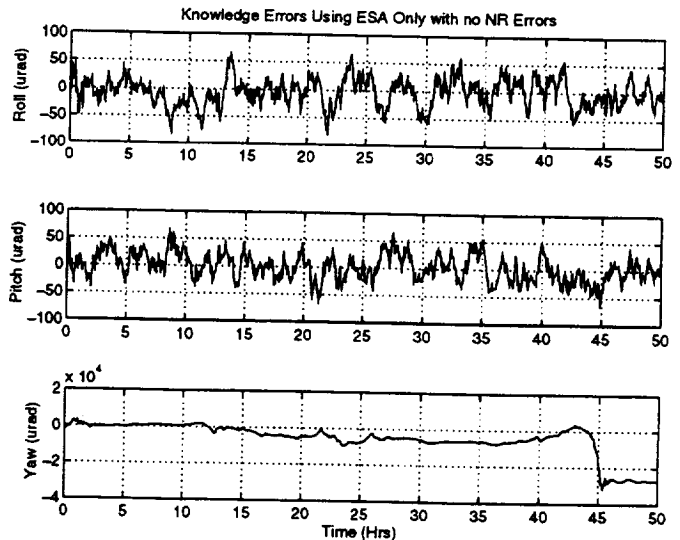


**Figure 2 Attitude Errors Using ESA with No Non-Repeatable Errors**

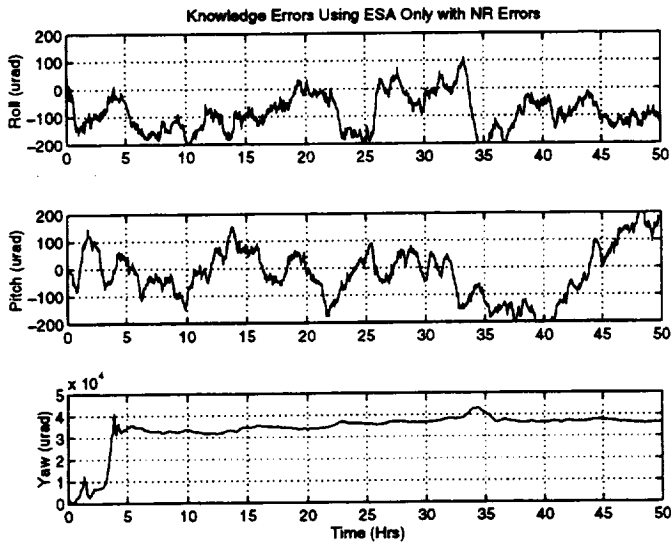


**Figure 3 Attitude Errors Using ESA with Non-Repeatable Errors**

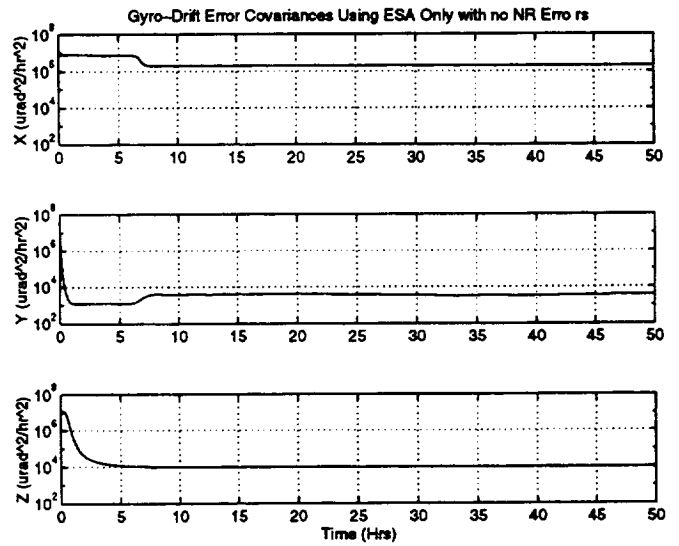


**Figure 5 Gyro Drift Covariance**

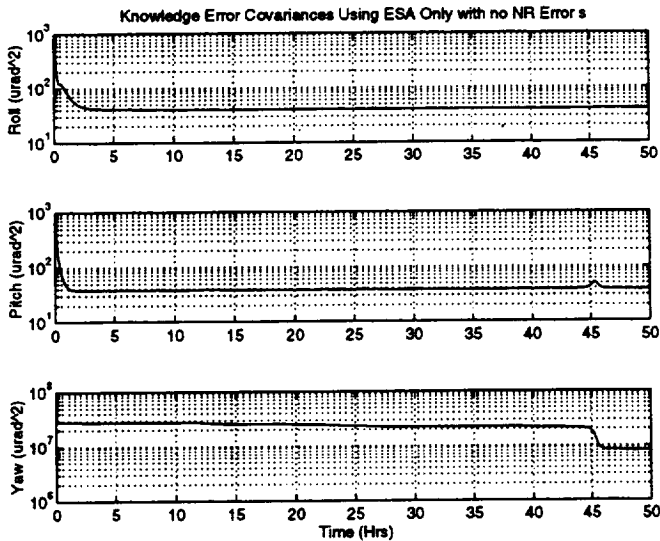


**Figure 4 Attitude Error Covariance**

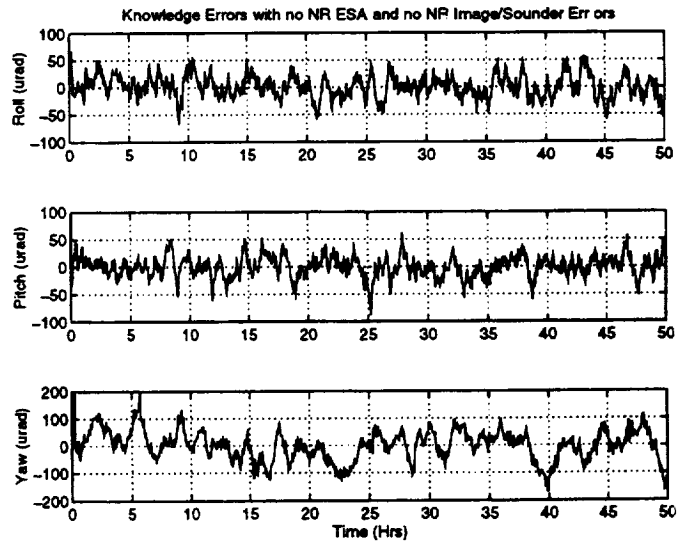


**Figure 6 Attitude Errors with No Non-Repeatable ESA Errors and No Non-Repeatable I/S Errors**

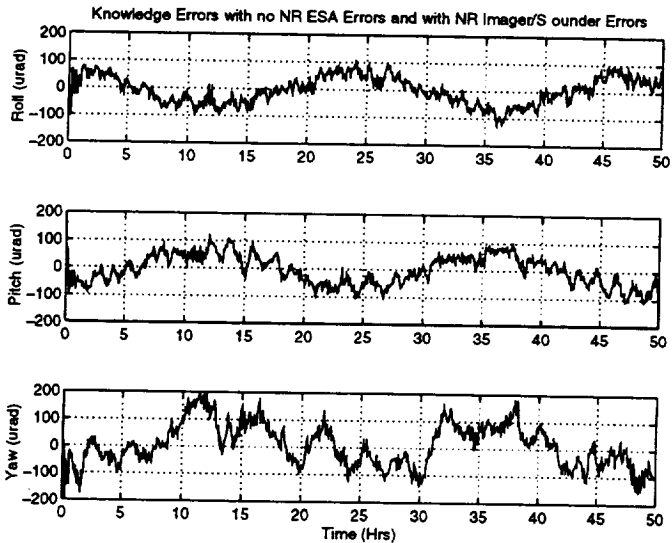


**Figure 7 Attitude Errors with No Non-Repeatable ESA Errors and with Non-Repeatable I/S Errors**

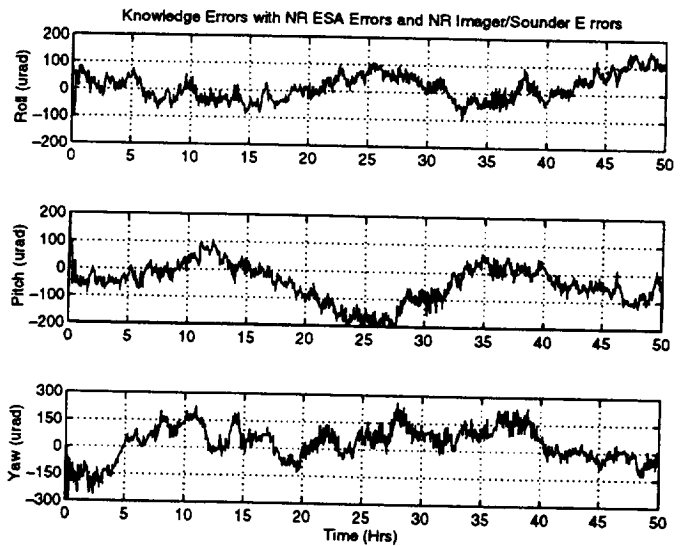


**Figure 9 Attitude Errors with Non-Repeatable ESA Errors and with Non-Repeatable I/S Errors**

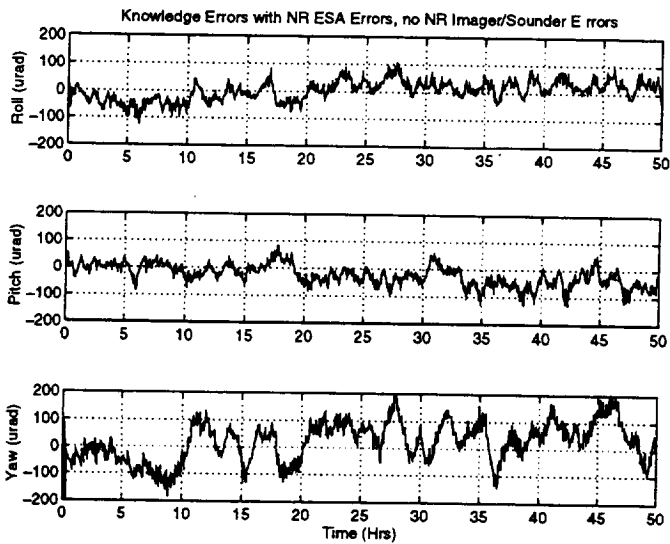


**Figure 8 Attitude Errors with Non-Repeatable ESA Errors and No Non-Repeatable I/S Errors**

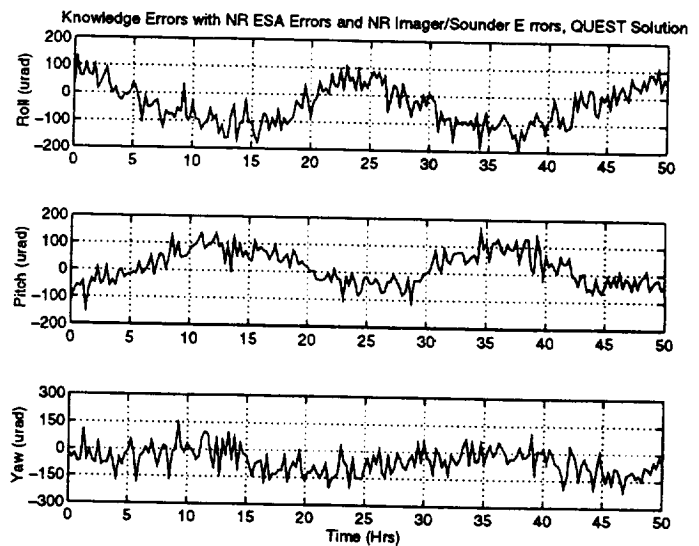


**Figure 10 Determined Attitude Errors Using QUEST**

## Star Tracker

In this section, the simulation results using a star tracker with and without gyros are presented. First, the star tracker model and parameters are shown. Then, a covariance analysis is presented in order to determine the optimal orientation of the star trackers. Next, the availability of actual stars for the GOES orbit is shown. Results are then presented using QUEST [4] to determine the spacecraft attitude. An Enhanced QUEST algorithm is also derived which filters sensor noise. Finally, simulation results are presented using gyros and a Kalman filter.

All results shown in this section include the dynamics and external disturbance in the spacecraft. The GOES Flight Software Dynamics Model implements the GOES AOCE firmware emulation FORTRAN code from the SS/L into a six degree of freedom dynamics model. The initial model was developed to examine the replacement of the ESA with gyros, and the current capability was developed to compare with actual GOES performance using the ESA. A star tracker and star tracker/gyro were also added into the simulation. The simulation includes rotating solar array inertia effects with fully coupled inertia tensor dynamics, magnetic torquers with ideal torque response, and gravity gradient and solar pressure disturbances.

The star tracker can sense up to six stars in an  $8^\circ \times 8^\circ$  field of view with a sampling interval of 0.1 seconds. The catalog contains stars which can be sensed up to a 6.0 magnitude. The star tracker measures the tangent of two angles,  $\beta_1$  and  $\beta_2$ , resulting in a body vector given by

$$\underline{B}_s = \frac{1}{\sqrt{1 + \tan^2 \beta_1 + \tan^2 \beta_2}} \begin{bmatrix} \tan \beta_1 \\ \tan \beta_2 \\ 1 \end{bmatrix} \quad (30)$$

where the z-axis of the star tracker is along the boresight. The star tracker "measurements" are obtained by using

$$\tan \tilde{\beta}_i = \tan \beta_i + v_s, \quad i = 1, 2 \quad (31)$$

where  $v_s$  is a zero-mean Gaussian process with a  $3\sigma$  value of 87.2665  $\mu\text{rad}$  (18 arc-sec).

Each star tracker must be positioned so that sun obtrusions can be avoided at all times. For the GOES orbit, and available sun shade for the star tracker, the minimum exclusion area (allowing for a  $3^\circ$  safety margin) is from  $55^\circ$  North to  $55^\circ$  South of the Nadir vector. For the single star tracker case, the  $55^\circ$  orientation produces the following order for knowledge accuracy: (1) roll angle (i.e., about the spacecraft's x-axis) is known most accurately, then (2) yaw angle (i.e., about the spacecraft's y-axis), and (3) pitch angle (i.e., about the spacecraft's z-axis) being the least accurate.

The roll is determined to be most accurate since the star tracker is perpendicular to this spacecraft's x-axis. Pitch accuracy cannot be improved since the  $55^\circ$  star tracker position leads to the y-axis being the least "orthogonal" axis with respect to the tracker boresight.

For the two tracker case, a covariance analysis was performed in order to determine the optimal orientation. Assuming that each star tracker measures one star for simplicity, the error covariance matrix is given by [5]

$$P = \frac{\sigma^2}{|b_1 \times b_2|^2} \left[ b_1 b_1^T + b_2 b_2^T + \frac{1}{2} (b_1 \times b_2)(b_1 \times b_2)^T \right] \quad (32)$$

where  $\sigma$  is the measurement error standard deviation, and  $b_1$  and  $b_2$  are measurement vectors of each star. For a North-South configuration, these measurement vectors are given by

$$b_1 = \begin{bmatrix} 0 \\ \sin 55^\circ \\ \cos 55^\circ \end{bmatrix} \equiv \begin{bmatrix} 0 \\ s \\ c \end{bmatrix} \quad (33a)$$

$$b_2 = \begin{bmatrix} 0 \\ -\sin 55^\circ \\ \cos 55^\circ \end{bmatrix} \equiv \begin{bmatrix} 0 \\ -s \\ c \end{bmatrix} \quad (33b)$$

Using Equation (33), the covariance in Equation (32) becomes

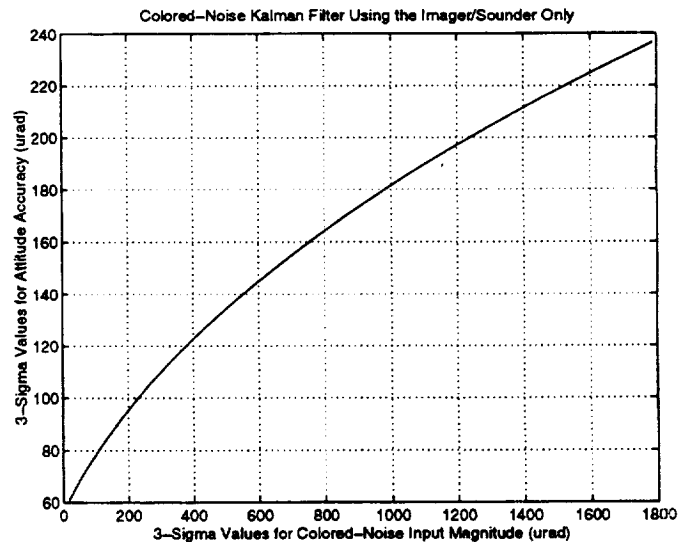


**Figure 11 Steady-State Colored-Noise Kalman Filter**

$$P = \frac{\sigma^2}{2} \begin{bmatrix} 1 & 0 & 0 \\ 0 & \frac{1}{c^2} & 0 \\ 0 & 0 & \frac{1}{s^2} \end{bmatrix} \quad (34)$$

The next configuration studied was to place the both star trackers 55° North (or South) from Nadir and separated by an angle  $\vartheta$ , The measurement vectors for this case are given by

$$b_1 = \begin{bmatrix} c\tilde{s} \\ s \\ c\tilde{c} \end{bmatrix}, \quad b_2 = \begin{bmatrix} -c\tilde{s} \\ s \\ c\tilde{c} \end{bmatrix} \quad (35)$$

where  $\tilde{s} \equiv \sin \vartheta$ , and  $\tilde{c} \equiv \cos \vartheta$ . The covariance matrix in Equation (32) for this case is given

$$P = \frac{\sigma^2}{2(c^4\tilde{s}^2\tilde{c}^2 + c^2\tilde{s}^2s^2)} \times \begin{bmatrix} c^2\tilde{s}^2 & 0 & 0 \\ 0 & s^2 + c^4\tilde{s}^2\tilde{c}^2 & cs\tilde{c} - c^3\tilde{s}^2\tilde{c}s \\ 0 & cs\tilde{c} - c^3\tilde{s}^2\tilde{c}s & c^2\tilde{c}^2 + c^2\tilde{s}^2s^2 \end{bmatrix} \quad (36)$$

In order to determine the optimal separation angle, a cost function involving roll and pitch errors (i.e., allowing for relaxed yaw error conditions) is defined, given by

$$J(\vartheta) = \frac{\sigma^2}{2(c^4\tilde{s}^2\tilde{c}^2 + c^2\tilde{s}^2s^2)} (c^2\tilde{s}^2 + s^2 + c^4\tilde{s}^2\tilde{c}^2) \quad (37)$$

Minimizing this cost function with respect to  $\vartheta$  leads to the optimal separation given by  $\vartheta = 90^\circ$ . Therefore, the covariance matrix in Equation (36) becomes

$$P = \frac{\sigma^2}{2} \begin{bmatrix} \frac{1}{s^2} & 0 & 0 \\ 0 & \frac{1}{c^2} & 0 \\ 0 & 0 & 1 \end{bmatrix} \quad (38)$$

Equation (38) shows that the yaw angle contains the smallest error, even though yaw was relaxed for the optimal separation angle. Therefore, comparing Equation (34) and Equation (38) leads to the conclusion that the optimal location for the two tracker case is given by one tracker 55° North and one tracker 55° South from Nadir.

## Simulation Results

Figure 12 shows the actual number of stars within the North pointing tracker field of view. There is always a minimum of 2 stars, except for the interval from 2.15 to 2.283 hours. A star with quality 1, but with a magnitude of 6.256, was added in this interval for the QUEST solution. Figure 13 shows the number of stars within the South pointing tracker field of view. A quality 2 star (5.137 magnitude) from the interval 15.45 to 15.483 hours, and another quality 1 star (6.138 magnitude) can be added to insure a minimum of two stars. This was not done to the South tracker catalog, since the North tracker was used for simulations involving one tracker. Figure 14 shows the combined number of stars for both trackers (without the addition of any stars). This shows that a minimum of 4 stars is available for the two tracker case. Also, the percentages of time in the orbit with the number of stars in the field of view are shown by Tables 2 and 3.

**Table 2 North Pointing Star Catalog**

Number of Stars	Percentage in FOV
0	0.0
1	0.625
2	10.972
3	15.625
4	27.709
5	23.958
6	21.111

**Table 3 South Pointing Star Catalog**

Number of Stars	Percentage in FOV
0	0.0
1	1.458
2	8.056
3	20.972
4	28.889
5	23.272
6	17.153

In this section simulation results using the QUEST and Enhanced QUEST algorithms without gyros are presented. The QUEST algorithm minimizes the following cost function

$$J(A) = \frac{1}{2} \sum_{k=1}^n \frac{1}{\sigma^2} |B_{s_k} - A I_{s_k}|^2 \quad (39)$$

where  $A$  is the attitude matrix, and  $n$  is the number of stars available. QUEST is a deterministic approach which utilizes a point-by-point solution. Therefore, previous measurements are not utilized in the attitude solution. This algorithm requires at least two star measurements to determine the attitude. Therefore, a star is added (as previously described) to the single star tracker case.

In general, the attitude knowledge is determined more accurately as the number of star measurements at one time increases and/or the separation distance between stars increases. This can be seen by the deterministic error covariance, given by [4]

$$P_{\hat{q}\hat{q}_k} = \sigma^2 \sum_{k=1}^n \left[ I_{3 \times 3} - \underline{B}_{s_k} \underline{B}_{s_k}^T \right]^{-1} \quad (40)$$

Figure 15 shows the attitude errors from QUEST determined attitude using a single (North) star tracker. Note the large errors about 2 hours into the simulation, which corresponds to the point where the star availability is mostly only 2 stars. Figure 15 also shows the attitude errors along with the  $3\sigma$  bounds from Equation (40). This shows excellent agreement between theory and simulation. Figure 16 shows the attitude errors using both star trackers. Figure 17 also shows the  $3\sigma$  bounds for the two star tracker case. This shows the significant improvement in attitude knowledge by using two trackers.

In order to further improve the attitude accuracy, an Enhanced QUEST algorithm (EQA) was developed. This is a simple first-order Kalman filter which combines a propagated model with the QUEST determined attitudes. Since gyros are not used for this case, the angular velocity is assumed to be perfect (i.e., given by Equation (6)). This assumption is not true, since external disturbances, and control and sensor errors are present in the actual system. Typical control errors using the ESA are shown in Figure 17. This shows the large errors and dynamic coupling in the roll/yaw axis. The EQA is given by

$$\hat{q}_{k+1}(-) = \exp\left\{\frac{1}{2}\Omega(\underline{\omega})\Delta t\right\} \hat{q}_k(+) \quad (41a)$$

$$\hat{q}_k(+) = (1-\alpha)\hat{q}_k(-) + \alpha \tilde{q}_k \quad (41b)$$

where  $\Delta t = 0.1$  seconds,  $\tilde{q}_k$  is the QUEST determined attitude at time  $t_k$ , and  $\alpha$  is a scalar gain. This gain was determined by minimizing the attitude errors from the simulated runs. A value which is too small adds too much model corrections, and tends to neglect measurements. A

value which is too large adds too much measurement noise, and tends to neglect model corrections. A value of  $\alpha = 0.05$  was determined to be optimal. The EQA covariance is derived by re-writing Equation (41) as

$$\hat{q}_{k+1} = \Phi_4 \hat{q}_k \otimes \left[ \underline{I} + \alpha \left( \left\{ \Phi_4 \hat{q}_k \right\}^{-1} \otimes \tilde{q}_{k+1} - \underline{I} \right) \right] \quad (42a)$$

$$\Phi_4 \equiv \exp\left\{\frac{1}{2}\Omega(\underline{\omega})\Delta t\right\} \quad (42b)$$

where  $\otimes$  denotes quaternion multiplication (see [1]). The QUEST determined quaternion is written as

$$\tilde{q}_{k+1} = \begin{bmatrix} \delta \tilde{q}_{k+1} \\ 1 \end{bmatrix} \otimes q_{k+1} \quad (43)$$

where  $q_{k+1}$  is the true quaternion, and  $\delta \tilde{q}_{k+1}$  is a three component error vector. Substituting Equation (43) into Equation (42a), and post-multiplying both sides of the resulting equation by  $q_{k+1}^{-1}$  yields

$$\hat{q}_{k+1} \otimes q_{k+1}^{-1} = \begin{bmatrix} \delta q_{k+1} \\ 1 \end{bmatrix} = \Phi_4 \hat{q}_k \otimes q_{k+1}^{-1} (1-\alpha) + \alpha \begin{bmatrix} \delta \tilde{q}_{k+1} \\ 1 \end{bmatrix} \quad (44)$$

Using a first-order approximation yields the following covariance covariance for the EQA

$$P_{\hat{q}\hat{q}_{k+1}} = (1-\alpha)^2 \Phi_3 P_{\hat{q}\hat{q}_k} \Phi_3^T + \alpha^2 P_{\tilde{q}\tilde{q}_k} \quad (45)$$

where  $\Phi_3$  is the state transition matrix of  $[\underline{\omega} \times]$ . Since this matrix is constant and nearly the identity matrix, the diagonal elements of Equation (45) approach the following steady-state

$$P_{\hat{q}\hat{q}_k} \approx \frac{\alpha}{2-\alpha} P_{\tilde{q}\tilde{q}_k} \quad (46)$$

Figure 18 shows the attitude errors and bounds from Equation (46) using one star tracker and the EQA. Comparing Figure 18 with Figure 15 shows a significant improvement using the EQA. Figure 19 shows the attitude errors using two trackers and the EQA. Comparing Figure 19 with Figure 16 again shows a significant improvement using the EQA.

In this section, the results using gyros and a Kalman filter are presented. Two gyro cases are simulated. The first case involves the utilization of the DRIRU-II. The second case involves the utilization of the of the HRG. The parameters for both gyros are summarized in Table 4.

**Table 4 Gyro Parameters**

Parameters	DRIRU-II	HRG
$\sigma_u$ (white noise)	$2.15 \times 10^{-4} \mu\text{rad}/\text{sec}^{3/2}$	$1.55 \times 10^{-4} \mu\text{rad}/\text{sec}^{3/2}$
$\sigma_v$ (random walk)	$0.206 \mu\text{rad}/\text{sec}^{1/2}$	$1.6 \mu\text{rad}/\text{sec}^{1/2}$

The gyro model is shown by Equations (1) and (2). The relative performance of the attitude estimation can be found by numerically iterating the Kalman filter equations to steady state, but Farrenkopf [3] obtained analytic solutions for the case when the three attitude error angles are assumed decoupled. Farrenkopf's results for the preupdate and postupdate attitude error standard deviations, denoted by  $\sigma(-)$  and  $\sigma(+)$ , respectively, can be written as

$$\sigma(-) = \sigma \left( \xi^2 - 1 \right)^{1/2} \quad (47a)$$

$$\sigma(+) = \sigma(-) / \xi \quad (47b)$$

where

$$\xi = \frac{1}{2} \left[ \gamma + \frac{1}{2} S_u + \left( \gamma S_u + S_v^2 + \frac{1}{3} S_u^2 \right)^{1/2} \right] \quad (48a)$$

$$\gamma = \left[ 4 + S_v^2 + (1/12) S_u^2 \right]^{1/2} \quad (48b)$$

$$S_u = \sigma_u \Delta t^{3/2} / \sigma \quad (48c)$$

$$S_v = \sigma_v \Delta t^{1/2} / \sigma \quad (48d)$$

In the limiting case of very frequent updates, the preupdate and the postupdate attitude error standard deviations both approach the continuous-update limit, given by

$$\sigma_\infty = \Delta t^{1/4} \sigma^{1/2} \left( \sigma_v^2 + 2\sigma_u \sigma_v \Delta t^{1/2} \right)^{1/4} \quad (49)$$

Using the parameters in Table 4 in Equation (49), it was determined that the DRIRU-II steady-state error is approximately 2.8 times better (i.e., more accurate) than the HRG. This is also shown in the simulations. Figures 20 and 21 show the attitude errors using the HRG for the one tracker and two tracker cases, respectively. Figures 22 and 23 show the attitude errors using the DRIRU-II for the one tracker and two tracker cases, respectively. Comparing Figure 20 to Figure 22, and Figure 21 to Figure 23, it is seen that the DRIRU-II is approximately 2 to 3 more accurate for the attitude knowledge than using the HRG. Results for the cases without gyros and cases with gyros are shown in Table 5 and Table 6, respectively.

**Table 5 Attitude Error Results Without Gyros**

Cases Simulated	Roll Error ( $\mu\text{rad}$ ) $3\sigma$	Pitch Error ( $\mu\text{rad}$ ) $3\sigma$	Yaw Error ( $\mu\text{rad}$ ) $3\sigma$
QUEST (1 Tracker)	60	1250	900
QUEST (2 Trackers)	35	70	50
EQA (1 Tracker)	12	225	175
EQA (2 Trackers)	6	10	8

**Table 6 Attitude Error Results With Gyros**

Cases Simulated	Roll Error ( $\mu\text{rad}$ ) $3\sigma$	Pitch Error ( $\mu\text{rad}$ ) $3\sigma$	Yaw Error ( $\mu\text{rad}$ ) $3\sigma$
KF, DRIRU-II (1 Tracker)	3	15	10
KF, DRIRU-II (2 Trackers)	2	3	2.5
KF, HRG (1 Tracker)	7	30	12
KF, HRG (2 Trackers)	5	9	7

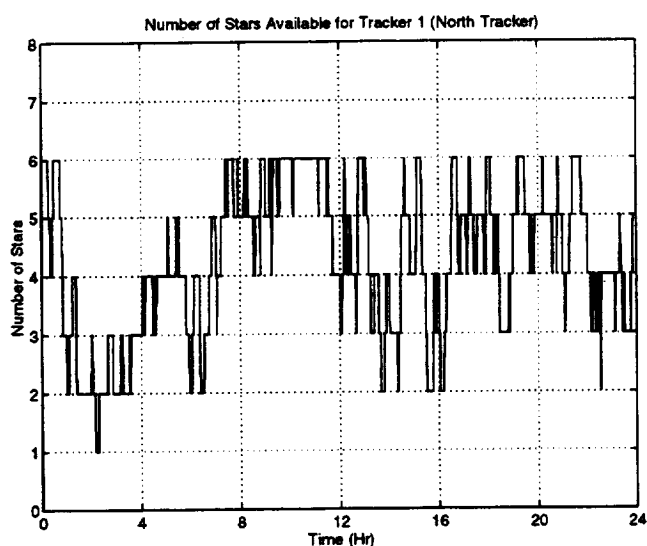


**Figure 12 Availability of Stars for the North Tracker**

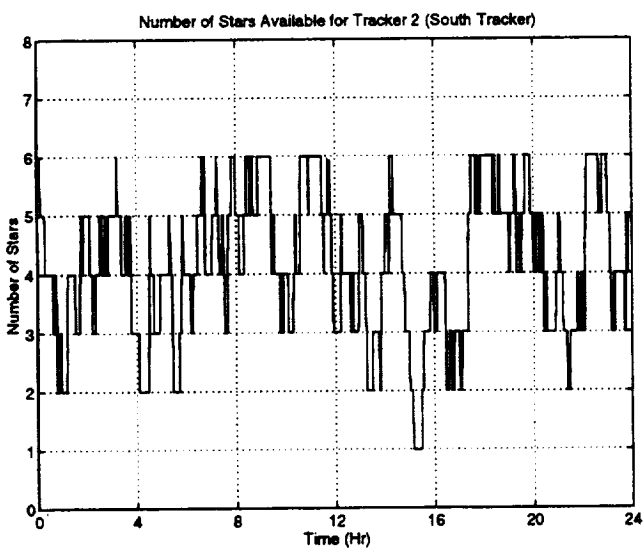


**Figure 13 Availability of Stars for the South Tracker**

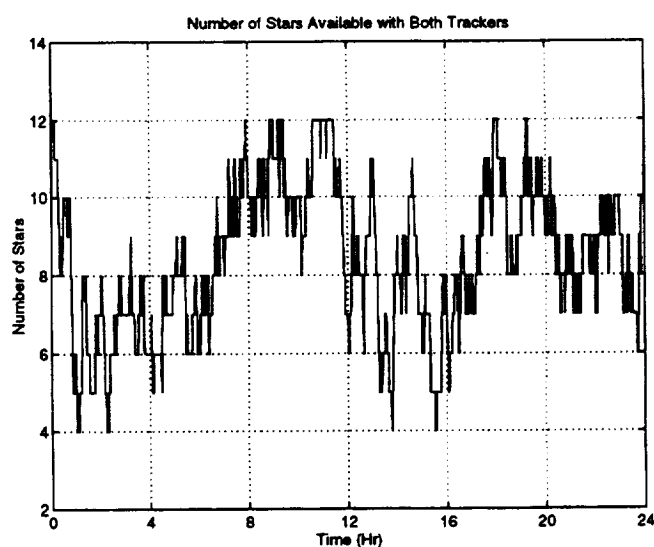


**Figure 14 Availability of Stars for Both Trackers**

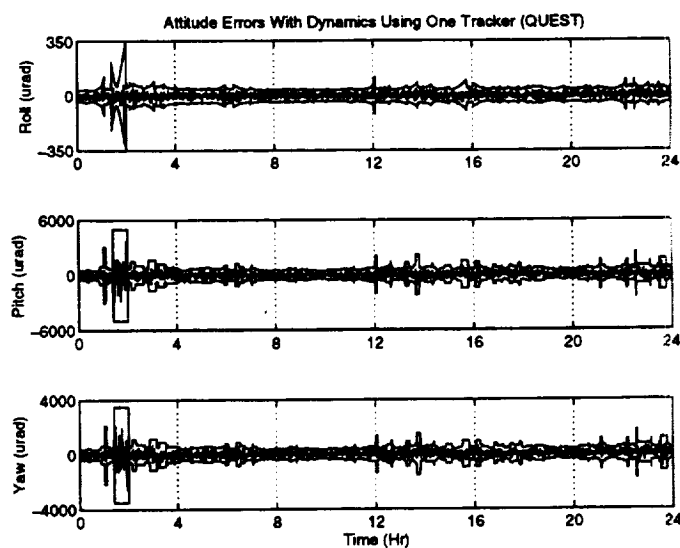


**Figure 15 Attitude Errors and Bounds Using One Tracker (QUEST)**

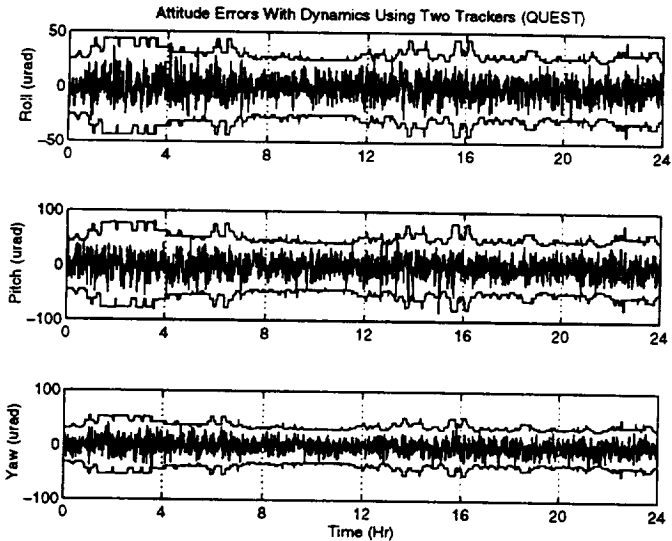


**Figure 16 Attitude Errors and Bounds Using Two Trackers (QUEST)**

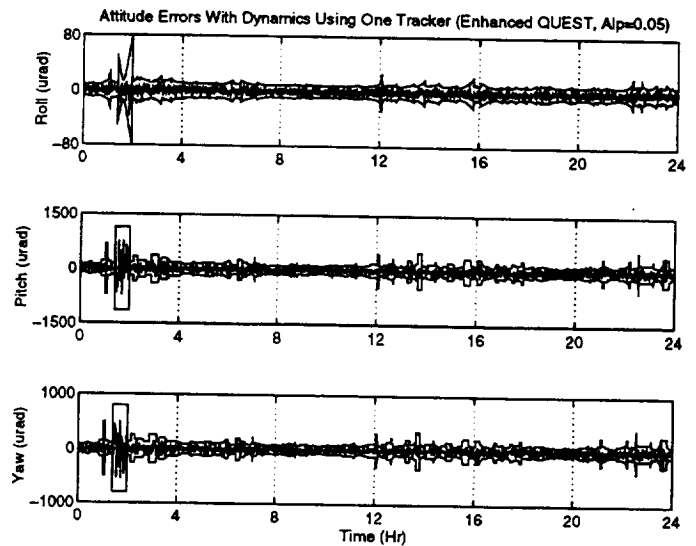


**Figure 18 Attitude Errors and Bounds Using One Tracker (Enhanced QUEST)**

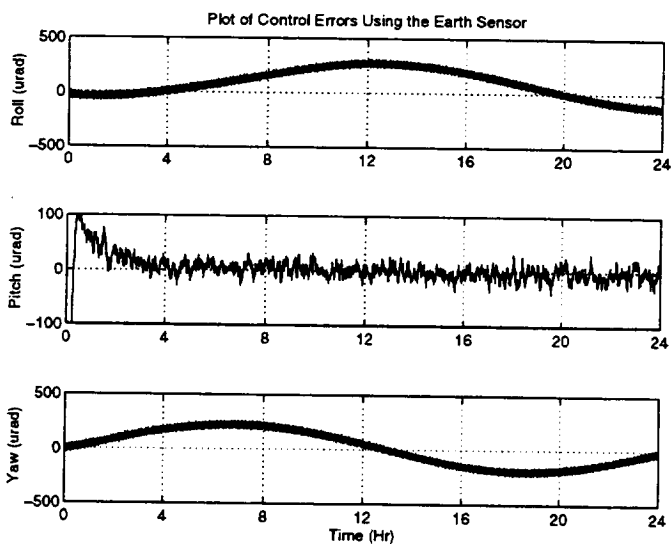


**Figure 17 Control Errors**

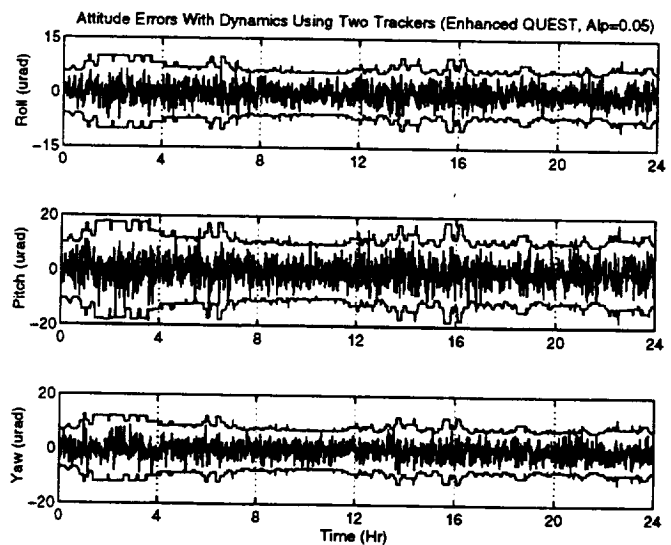


**Figure 19 Attitude Errors Using Two Trackers (Enhanced QUEST)**

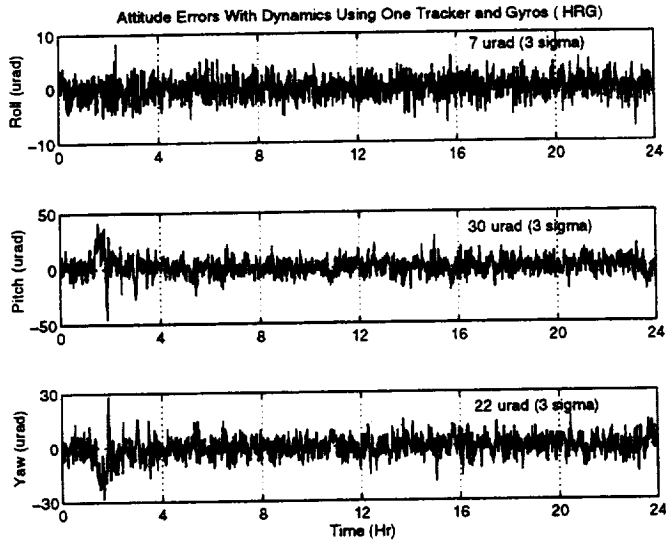


**Figure 20 Attitude Errors Using One Tracker (Kalman Filter, HRG)**

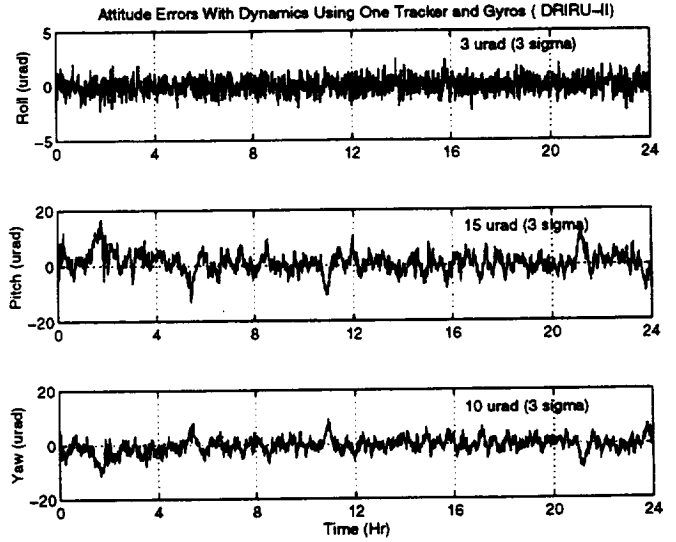


**Figure 22 Attitude Errors Using One Tracker (Kalman Filter, DRIRU-II)**

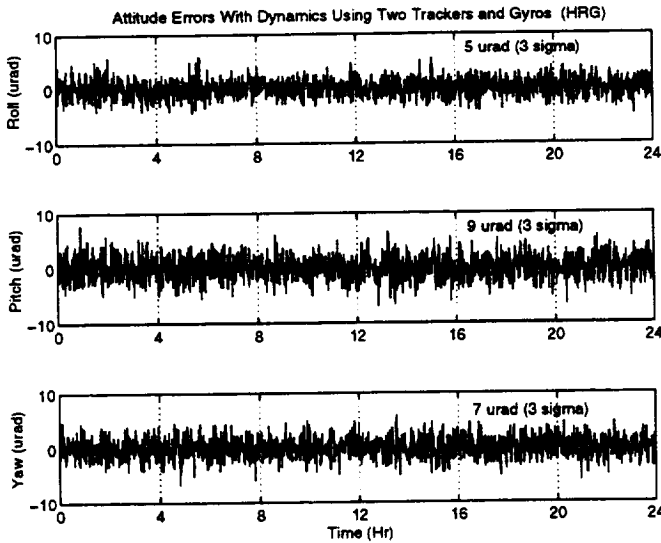


**Figure 21 Attitude Errors Using Two Trackers (Kalman Filter, HRG)**

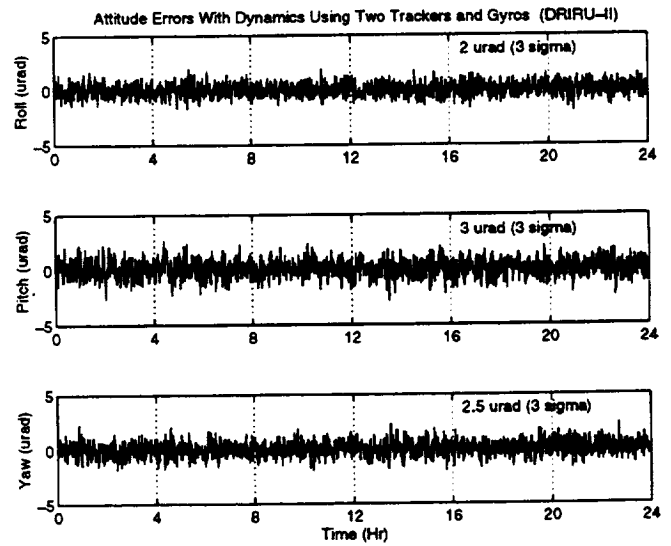


**Figure 23 Attitude Errors Using Two Trackers (Kalman Filter, DRIRU-II)**

## Conclusions

This study provided some insightful information for using gyros on the GOES spacecraft. It was determined that the gyros do not significantly reduce the non-repeatable errors in the ESA. This was shown by comparing Figure 9 with Figure 10. Since the relative error is approximately equal in these two plots, we conclude that the utilization of on-board gyros does not significantly improve performance. Also, using gyros does not provide any observability in the yaw angle estimate, when using the ESA.

The star tracker simulation results show a significant improvement over the ESA attitude knowledge errors. The greatest improvements were showing using either: (1) two trackers with the EQA, or (2) one tracker and a DRIRU-II type gyro, and (3) two trackers and either an HRG type gyro or a higher quality gyro such as the DRIRU-II. Adding gyros to the spacecraft is the most ideal case since the filter bandwidth is larger than the EQA filter bandwidth (i.e., the Kalman filter with gyros can sense higher frequency spacecraft motions than an EQA). The utilization of on-board gyros may also improve the pointing accuracy, since the controller bandwidth may be increased.

## Acknowledgments

The first author's work was supported by a National Research Council Postdoctoral Fellowship tenured at NASA-Goddard Space Flight Center. The author greatly appreciates this support. Also, the authors wish to thank Jim Kaidy for provided the dynamic simulation for the GOES spacecraft.

## References

- [1] Lefferts, E.J., Markley, F.L., and Shuster, M.D., "Kalman Filtering for Spacecraft Attitude Estimation," *Journal of Guidance, Control and Dynamics*, Vol. 5, No. 5, Sept.-Oct. 1982, pp. 417-429.
- [2] Wertz, J.R., (editor) *Spacecraft Attitude Determination and Control*, Kluwer Academic Publishers, Dordrecht, 1978.
- [3] Farrenkopf, R.L., "Analytic Steady-State Accuracy Solutions for Two Common Spacecraft Attitude Estimators," *Journal of Guidance and Control*, Vol. 1, July-Aug. 1978, pp. 292-284.
- [4] Shuster, M.D., and Oh, S.D., "Three-Axis Attitude Determination from Vector Observations," *Journal of Guidance and Control*, Vol. 4, No. 1, Jan.-Feb. 1981, pp. 70-77.
- [5] Markley, F.L., "Attitude Determination Using Vector Observations: A Fast Optimal Matrix Algorithm," *Journal of the Astronautical Sciences*, Vol. 41, No. 2, April-June 1993, pp. 261-280.
- [6] Markley, F.L., Bauer, F.H., Deily, J.J., and Femiano, M.D., "Attitude Control System Conceptual Design for the Geostationary Operational Environmental Satellite Spacecraft Series," *Journal of Guidance, Control, and Dynamics*, Vol. 18, No. 2, March-April 1995, pp. 247-255.

